Physics in Medicine & Biology

IPEM Institute of Physics and Engineering in Medicine

PAPER • OPEN ACCESS

# Motion-robust magnetic resonance fingerprinting (MR-MRF) for quantitative liver cancer imaging

To cite this article: Chenyang Liu *et al* 2026 *Phys. Med. Biol.* **71** 035015

View the article online for updates and enhancements.

You may also like

- A novel reconstruction method based on basis function decomposition for snapshot CAXRDT system
Shengzi Zhao, Le Shen, Donghang Miao et al.
- Deep radiomics for prognostic prediction in locally advanced non-small cell lung cancer by leveraging OmicsMap-based image representation
Runping Hou, Wuyan Xia, Md Tauhidual Islam et al.
- Design optimization using GATE Monte Carlo simulations for a sub-0.5 mm resolution PET scanner with 3-layer DOI detectors
Han Gyu Kang, Hideaki Tashima, Makoto Higuchi et al.

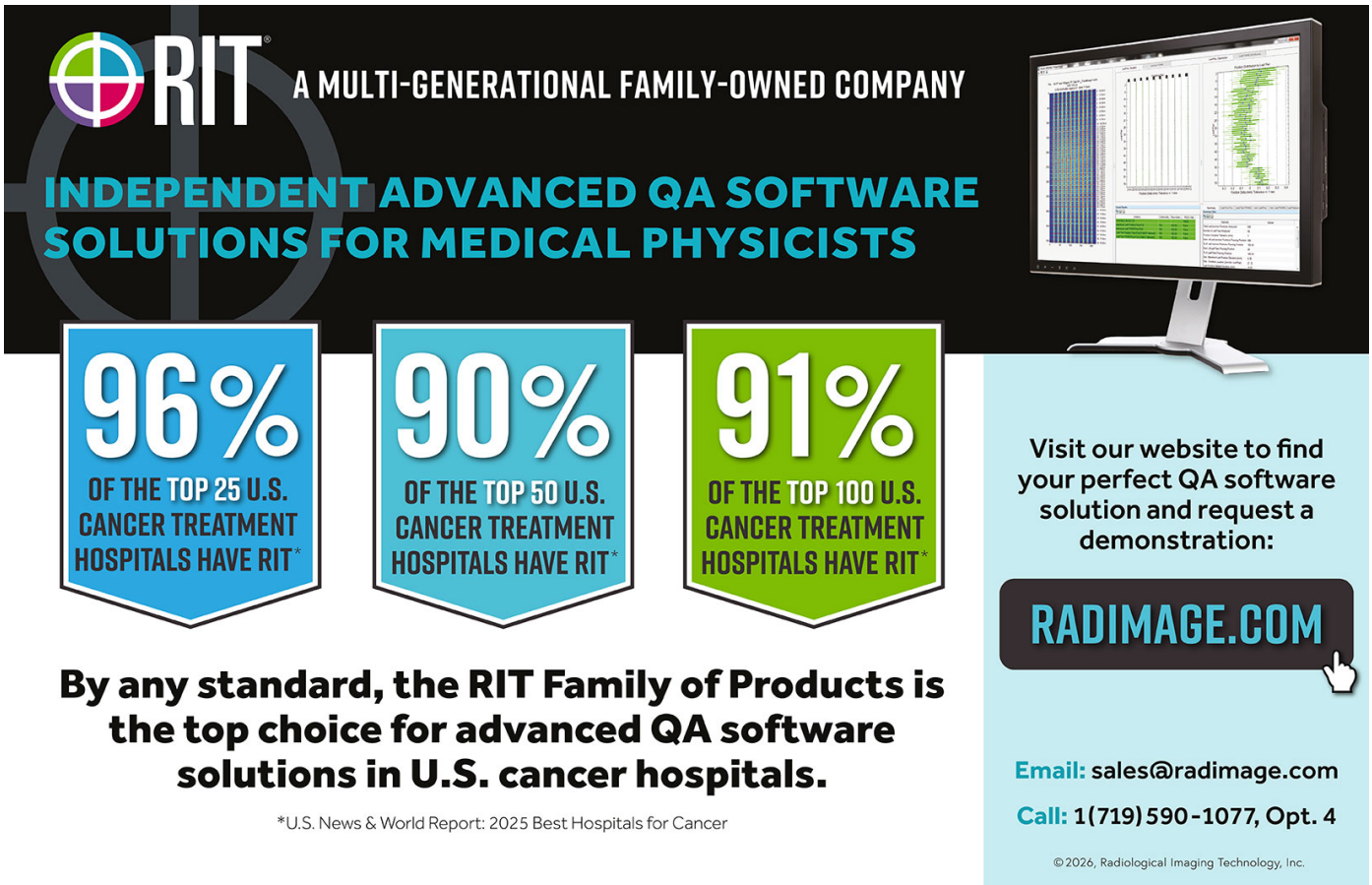


This content was downloaded from IP address 158.132.161.180 on 11/03/2026 at 02:18

IOP Publishing Phys. Med. Biol. 71 (2026) 035015 https://doi.org/10.1088/1361-6560/ae3b03

Physics in Medicine & Biology

IPEM Institute of Physics and Engineering in Medicine

Check for updates

PAPER

# Motion-robust magnetic resonance fingerprinting (MR-MRF) for quantitative liver cancer imaging

**Chenyang Liu[1], Tian Li[1], Lu Wang[1,2], Yat-Lam Wong[3], Mandi Wang[4], Huiqin Zhang[5], Zuojun Wang[6], Haonan Xiao[7], Shaohua Zhi[1,8], Wen Li[1], Jiang Zhang[1], Xinzhi Teng[1], Victor Ho-fun Lee[3], Peng Cao[6] and Jing Cai[1,9,*]**

[1] Department of Health Technology and Informatics, The Hong Kong Polytechnic University, Hong Kong Special Administrative Region of China, People's Republic of China
[2] College of Information Science and Engineering, Northeastern University, Shenyang, People's Republic of China
[3] Department of Clinical Oncology, Queen Mary Hospital, Hong Kong Special Administrative Region of China, People's Republic of China
[4] Department of Radiology, Shenzhen People's Hospital, Shenzhen, People's Republic of China
[5] Department of Diagnostic Radiology, Cancer Hospital, Chinese Academy of Medical Sciences and Peking Union Medical College, Beijing, People's Republic of China
[6] Department of Diagnostic Radiology, The University of Hong Kong, Hong Kong Special Administrative Region of China, People's Republic of China
[7] Department of Radiation Oncology and Physics, Shandong Cancer Hospital and Institute, Jinan, Shandong, People's Republic of China
[8] Wu Jieh Yee School of Interdisciplinary Studies, Lingnan University, Hong Kong Special Administrative Region of China, People's Republic of China
[9] Research Institute for Smart Ageing, The Hong Kong Polytechnic University, Hong Kong Special Administrative Region of China, People's Republic of China
[*] Author to whom any correspondence should be addressed.

**E-mail:** jing.cai@polyu.edu.hk

**Keywords:** magnetic resonance imaging, magnetic resonance fingerprinting, liver cancer, respiratory motion blurring, motion robust

OPEN ACCESS

RECEIVED
24 September 2025

REVISED
9 January 2026

ACCEPTED FOR PUBLICATION
20 January 2026

PUBLISHED
10 February 2026

Original content from this work may be used under the terms of the Creative Commons Attribution 4.0 licence.

Any further distribution of this work must maintain attribution to the author(s) and the title of the work, journal citation and DOI.

## Abstract

*Objective.* This study aims to develop a motion-robust magnetic resonance fingerprinting (MR-MRF) technique for liver cancer imaging to eliminate the need for breath-hold scanning. *Approach.* To mitigate respiratory motion artifacts in free-breathing abdominal MRF, the MR-MRF technique comprising two core components. First, respiratory motion is modeled by applying an isotropic total variation (TV)-regularized registration algorithm between a target end-of-exhalation (EOE) phase and three motion phases. Second, motion-resolved tissue property maps are reconstructed using a low-rank TV optimization framework, which incorporates the estimated inter-phase motion to align all acquired MRF dynamics to the EOE phase. MR-MRF is evaluated by 22 patients (mean age, 62 years ± 10 [SD]; 15 males and 7 females) with hepatocellular carcinoma. Radiologist's blinded assessment and organ boundary sharpness measurements are performed to evaluate the image quality of MR-MRF-derived tissue maps. The test-retest tissue quantification repeatability is assessed by two consecutive MRF scans with distinct breathing patterns. Paired Student's *t*-test is used for statistical significance analysis with a *p*-value threshold of 0.05. *Main results.* MR-MRF achieved successful reconstruction of motion-resolved tissue maps at EOE phase, with blinded radiologist assessment yielding an average score of 3 (moderate quality—sufficient for diagnosis) for overall image impression. The FWHM of organ boundaries in MR-MRF-derived tissue maps is 3.1 mm ± 1.7 mm, significantly lower than motion-blurred tissue maps (9.9 mm ± 3.4 mm, $p$-value $< 0.0001$). Test-retest analysis demonstrated good repeatability: liver coefficient of variation was 5.5% ± 7.1% (T1), 8.2% ± 4.4% (T2), and 5.0% ± 2.0% (PD), with excellent linear agreement ($R^2 = 0.96$, 0.80, and 0.85 for T1, T2, and PD, respectively). *Significance.* This study establishes the technical foundation of MR-MRF to achieve repeatable and quantitative liver T1/T2/PD mapping under free-breathing conditions at 3 T. The results validate the feasibility of addressing respiratory motion in abdominal multi-parametric quantitative MRI.

© 2026 The Author(s). Published on behalf of Institute of Physics and Engineering in Medicine by IOP Publishing Ltd

## 1. Introduction

Magnetic resonance fingerprinting (MRF) is an innovative quantitative MRI technique capable of simultaneously measuring multiple tissue properties, such as T1/T2 relaxation times and proton density (PD), in a single acquisition (Ma *et al* 2013, Poorman *et al* 2020). MRF utilizes consecutive radiofrequency (RF) pulses with varying parameters to generate unique temporal signal evolutions that encode intrinsic tissue properties. The feasibility of MRF for quantitative abdominal imaging has been established in a number of studies. Chen *et al* (2016) found MRF could differentiate focal liver lesions from surrounding healthy tissue by exhibiting different T1 and T2 values ($p$-value $< 0.01$) (Chen *et al* 2016). Jaubert *et al* (2020) demonstrated substantial agreement between MRF-derived tissue maps and conventional quantitative MRI approaches (Jaubert *et al* 2020). Fujita *et al* (2022) further reported correlations between MRF and liver biopsy findings in diffuse liver disease (Fujita *et al* 2022). Additionally, abdominal MRF has shown high repeatability (3.2%–7.1%, coefficient of variation) and reproducibility (less than 3% variation) (MacAskill *et al* 2021, Fujita *et al* 2022).

While abdominal MRF has demonstrated promising diagnostic performance, a technical limitation hinders its broader clinical implementation. Current MRF implementations typically require extended acquisition periods (14–19 s per 2D slice) due to the need for lengthy RF pulse sequences ($\geqslant$1000 repetitions) to achieve sufficient tissue-specific signal differentiation (Jiang *et al* 2015). This prolonged scan duration necessitates breath-holding to mitigate respiratory motion artifacts (Chen *et al* 2016, Jaubert *et al* 2020, MacAskill *et al* 2021, Fujita *et al* 2022). However, this breath-hold requirement poses challenges, particularly for patients with respiratory difficulties. To address the respiratory motion-induced artifacts, several motion-resolved MRF techniques have been developed, allowing for free-breathing MRF acquisition. Li *et al* (2020) and Huang *et al* (2021) have adopted a retrospective sorting approach where the MRF signals are sorted into different motion phases, and the corresponding motion-free tissue maps are reconstructed independently (Li *et al* 2020, Huang *et al* 2021). Besides, motion modeling has been used to eliminate the motion artifacts by deforming the MRF signals acquired from different motion phases into one target phases (Cruz *et al* 2021, Cao *et al* 2022). However, all current motion-resolved methods are subjective to suboptimal image quality and have only been validated on healthy volunteers. The performance of motion-resolved MRF methods on abdominal patients and their robustness to respiratory motion remain to be investigated.

In this prospective study, we developed a novel motion-robust MRF (MR-MRF) technique for improved liver tissue property mapping. MR-MRF incorporates two innovations to mitigate respiratory motion-induced artifacts, including a respiratory motion modeling method and an iterative motion-corrected tissue map optimization method. The performance and robustness of MR-MRF to respiratory motion is evaluated through image quality metrics and tissue property quantification repeatability, utilizing a cohort of 22 hepatocellular carcinoma patients. To the best of our knowledge, this study represents the first clinical investigation to demonstrate the feasibility multi-parametric quantitative liver cancer imaging under free-breathing conditions.

## 2. Materials and methods

The MRF study consists of digital phantom studies and *in vivo* studies. The *in vivo* studies were approved by the institutional review board. Written consent was collected from all participants.

### 2.1. MRF acquisition

The MRF experiments were performed on a 3.0T-MRI scanner (SIGNA Premier, GE Healthcare). Data were acquired using a two-dimensional fast acquisition with steady-state precession (FISP) sequence with highly under-sampled spiral readouts (Jiang *et al* 2015). A schematic illustration of the MRF acquisition scheme is shown in figure 1(a). The sequence used 1000 consecutive RF pulses with echo times of 1.77 ms, and pseudo-random flip angles from 0° to 70° and repetition time from 11.7 to 14.3 ms. The spiral trajectory was implemented in the sagittal plane, with the FISP sequence repeated in the medial-lateral direction to achieve 3D $k$-space coverage. The in-plane field of view is 300 $\times$ 300 mm$^2$ and the resolution is 256 $\times$ 256.

### 2.2. MR-MRF image reconstruction

The MRF $k$-space data was exported by the GE research toolbox and reconstructed offline in Matlab (R2021b, MathWorks) using a self-developed MR-MRF toolbox. As illustrated by figure 1(b), this toolbox incorporates two components to mitigate respiratory motion-induced artifacts, including respiratory motion modeling and motion-resolved tissue map optimization.

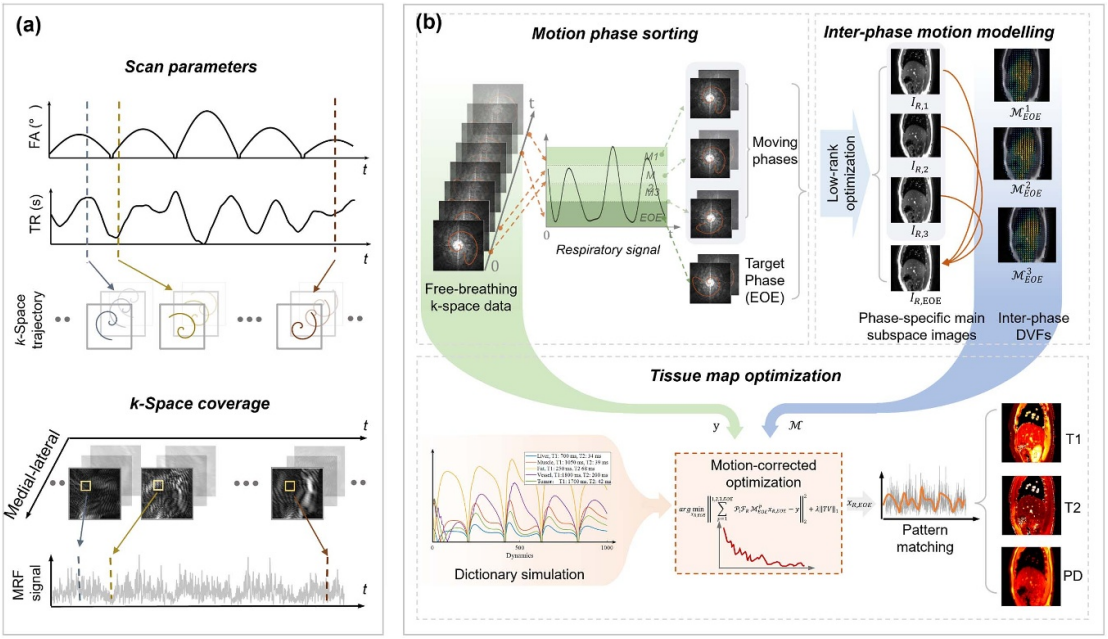


**Figure 1.** Schematic illustration of MRF acquisition and MR-MRF image reconstruction. (a) The steady-state precession (FISP) pulse sequence for MRF acquisition. (b) The MR-MRF image reconstruction toolbox. The free-breathing *k*-space data was retrospectively sorted into a target end-of-exhalation (EOE) phases and three additional moving phases based on the amplitude respiratory surrogate. Motion-state subspace images ($I_1$, $I_2$, $I_3$, and $I_{\mathrm{EOE}}$) are reconstructed for motion modeling, obtaining inter-phase DVFs ($\mathcal{M}^1_{\mathrm{EOE}}$, $\mathcal{M}^2_{\mathrm{EOE}}$, and $\mathcal{M}^3_{\mathrm{EOE}}$). Then, a motion-compensated reconstruction framework is performed to obtain $x_{\mathrm{R,EOE}}$, which is the subspace image of EOE phase that is full sampled in the subspace domain. Finally, pattern matching is performed on $x_{\mathrm{R,EOE}}$ to obtain the motion-resolved tissue maps.

### *2.2.1. Respiratory motion modeling*

The free-breathing *k*-space data was retrospectively sorted into a target end-of-exhalation (EOE) phases and three additional moving phases based on the amplitude respiratory surrogate. After phase sorting, the respiratory motion from moving phases to target phase was modeled by deformation vector fields (DVFs). The DVFs were calculated motion-state subspace images derived from phase-specific *k*-space data using the inverse low-rank Fourier Transform (Assländer *et al* 2018). As the *k*-space data is highly under-sampled, a low-rank total variation (LRTV) optimization method (McGivney *et al* 2014, Golbabaee *et al* 2021) was applied to obtain the phase-specific subspace images for DVF calculation, as defined in equation (1),

$$\arg\min_{I_{\mathrm{R,P}}} \|\mathcal{P}_{\mathrm{i}}\left(\mathcal{F}_{\mathrm{R}} I_{\mathrm{R,i}} - y\right)\|_2^2 + \lambda \|\mathrm{TV}\|_1 \,\mathrm{for}\, i = 1,2,3,\mathrm{EOE} \tag{1}$$

where $y$ is the *k*-space MRF data, $\mathcal{P}_{\mathrm{i}}$ represents the phase sorting mask of either target phase ($\mathcal{P}_{\mathrm{EOE}}$) or moving phases ($\mathcal{P}_1$, $\mathcal{P}_2$ and $\mathcal{P}_3$), $\mathcal{F}_{\mathrm{R,i}}$ is the low-rank non-uniform Fast Fourier transform (NUFFT), $I_i$ is the optimized phase-specific subspace image for moving or target phases, and TV was used to enforce the data sparsity (Wang *et al* 2016, Assländer *et al* 2018).

The optimized main subspace images for each motion phases were used for respiratory motion modeling. Specifically, three inter-phase DVFs—denoted as $\mathcal{M}^1_{\mathrm{EOE}}$, $\mathcal{M}^2_{\mathrm{EOE}}$, and $\mathcal{M}^3_{\mathrm{EOE}}$ —were calculated, defined as the displacement maps from the EOE phase to motion phases 1, 2, and 3, respectively. The DVF were calculated by an isotropic TV-regularized registration algorithm, which is particularly suited for parameterizing non-smooth sliding motion between the liver and body cavities (Vishnevskiy *et al* 2017).

### *2.2.2. Motion-resolved tissue map optimization*

A motion-compensated reconstruction framework based on a LRTV optimization algorithm was developed to generate motion-resolved tissue maps. The tissue optimization is defined by equation (2),

$$\arg\min_{x_{\mathrm{R,EOE}}} \left\| \sum_{p=1}^{1,2,3,EOE} \mathcal{P}_{\mathrm{i}} \mathcal{F}_R \mathcal{M}^{\mathrm{p}}_{EOE} x_{\mathrm{R,EOE}} - y \right\|_2^2 + \lambda \|\mathrm{TV}\|_1 \tag{2}$$

where $\mathcal{F}_{\mathrm{R}}$ represents the low-rank NUFFT and $x_{\mathrm{EOE}}$ is the motion-compensated subspace images for the

**Table 1.** Patient characteristics.

| Characteristics | Value |
|---|---|
| Number of patients (n) | 22 |
| Female | 7 |
| Male | 15 |
| Patient age (mean ± SD [range]) | 61.6 ± 9.5 [41–86] |
| Female | 66.7 ± 9.6 [53–86] |
| Male | 59.2 ± 8.5 [41–77] |
| Cancer type | Hepatocellular carcinoma (HCC) |
| MRF scan types | |
| Pre-treatment scans | 12 |
| Three-month follow-up scans | 12 |
| Six-month follow-up scans | 3 |

Abbreviation: SD = standard deviation.

EOE phase. Compared to equations (1) and (2) incorporates an additional parameter—the inter-phase DVFs ($\mathcal{M}^{\mathrm{p}}_{\mathrm{EOE}}$) calculated in section 2.2.1. It is important to note that while both $x_{\mathrm{R,EOE}}$ in equation (2) and $I_{\mathrm{R,i}}$ in equation (1) are subspace images reconstructed using the LRTV algorithm, they differ fundamentally in their data sources. The term $I_{\mathrm{R,i}}$ is derived from the phase-specific *k*-space data, representing motion-state subspace images, which are under-sampled in the subspace domain. In contrast, $x_{\mathrm{R,EOE}}$ is reconstructed by all acquired *k*-space data across respiratory phases to achieve full sampling in the subspace domain. To obtain motion-resolved $x_{\mathrm{R,EOE}}$ from free-breathing *k*-space data, the inter-phase DVFs deform the $x_{\mathrm{R,EOE}}$ to each moving phase ($x_{R,1}$, $x_{R,2}$, $x_{R,3}$) in equation (2). This step incorporates physiological motion information. The $\mathcal{F}_R$ convert these motion-state fully sampled subspace images to corresponding full rank k-space data. Finally, $\mathcal{P}_{\mathrm{i}}$ are applied and the masked k-space data of each phase are summed to synthesize the composite k-space data $y$ acquired during free breathing. Thus, the forward process of equation (2) approximates the measured free-breathing *k*-space data using only the subspace images of the target phase, $x_{\mathrm{R,\,EOE}}$, enabling its iterative optimization within the reconstruction framework.

The MRF dictionary was simulated using the Bloch equation, followed by a pattern matching operation on $x_{\mathrm{R,\,EOE}}$ to reconstruct the tissue maps (Weigel 2015). The dictionary table contains 113 781 entries, with T1 relaxation times from 10 to 4000 ms and T2 times from 10 to 1000 ms.

The MR-MRF reconstruction toolbox was implemented on a GPU workstation (NVIDIA RTX 3090) to accelerate the computationally intensive NUFFT and pattern matching operations. The processing time was approximately 1.5 min per motion-resolved 2D tissue map. Complete volume-wise reconstruction required 15–30 min in total, a duration dependent on the number of acquired 2D slices per patient.

### 2.3. Digital phantom MRF studies

A phantom study was performed on ten whole-body digital phantoms. The phantoms were simulated by the extended cardiac-torso phantom under different parameter settings, such as gender, heights, weights, volumes of the organ, maximum diaphragm motion range, and respiratory signal pattern (Segars *et al* 2010, Panta *et al* 2012, Segars *et al* 2018). Each digital phantom underwent 10 repeated MRF. Irregular respiratory motion profiles were applied to each simulated MRF scan to better approximate real physiological conditions. These profiles were generated using a sinusoidal waveform base, but with two key varying parameters to introduce irregularity: (1) respiratory period randomly varied between 3–6 s, and (2) maximum diaphragm displacement randomly varied between 1–3 cm.

### 2.4. *In vivo* MRF studies

The in vivo studies were conducted over a 40 month period, from June 2, 2021 to August 8, 2024. A total of 22 hepatocellular carcinoma patients were included in the *in vivo* MRF study. The demographic characteristics of the patient cohort are summarized in table 1. MRF imaging was performed on the patient cohort either prior to treatment, after treatment, or at both timepoints, resulting in 27 MRF scan cases. For each MRF scan acquisition, 2 consecutive free-breathing MRF scans were obtained to assess tissue property quantification test-retest repeatability. No respiratory training or controlled breathing instructions were provided to the participants during the repeated MRF measurements. Immediately following the MRF scan sequence, conventional MRI scans, including T1-weigthed MRI, contrast-enhanced (CE) MRI, and diffusion-weighted MRI, are performed for HCC cancer patients.

**Table 2.** Grade table of the image quality blinded assessment.

| | Grade | Description |
|---|---|---|
| Overall image impression | 1 | Unacceptable, no diagnosis possible |
| | 2 | Inconclusive, diagnosis confidence substantially reduced |
| | 3 | Moderate, sufficient for diagnosis |
| | 4 | Good |
| | 5 | Excellent |
| Noises | 1 | Unacceptable |
| | 2 | Definitely noisy |
| | 3 | Slightly noisy, but acceptable |
| | 4 | Minimal noise, not affecting diagnostic quality |
| | 5 | No perceivable noise |
| Artifacts | 1 | Severe artifact |
| | 2 | Moderate artifact, degrading diagnostic capability |
| | 3 | Slight artifact, not interfering with diagnosis capability |
| | 4 | Minimal artifact |
| | 5 | No perceivable artifact |
| Sharpness | 1 | Very poor, poorly visualized anatomy structures |
| | 2 | Poor, liver boundary is blurred by respiratory motion |
| | 3 | Inconclusive, fairly delineated liver boundary |
| | 4 | Good, good delineation of liver with a sharp boundary |
| | 5 | Excellent, excellent sharpness of the liver. |
| Vascular conspicuity | 1 | Not recognizable |
| | 2 | Blurry but visualized |
| | 3 | Acceptable |
| | 4 | Distinct signal difference |
| | 5 | Distinct signal difference with a sharp vascular margin |
| Lesion conspicuity | 1 | Not recognizable |
| | 2 | Blurry but visualized |
| | 3 | Acceptable |
| | 4 | Distinct signal difference |
| | 5 | Distinct signal difference with a sharp lesion margin |

### 2.5. Statistical analysis

Two experienced radiologists independently evaluated MR-MRF-derived motion-resolved tissue maps across six parameters: overall image quality, noise, artifacts, sharpness, vascular conspicuity, and lesion conspicuity (grading scale detailed in table 2). In a blinded reader study, radiologists' quality ratings of motion-resolved tissue maps were compared against those of motion-blurred tissue maps reconstructed directly from the free-breathing MRF signals without MR-MRF post-processing. In addition, the performance of motion correction was assessed by the sharpness of the organ boundaries and was quantified by the full-width half maximum (FWHM) of the lung-liver boundary (Xiao *et al* 2022). Linear profiles were drawn at the liver-lung interfaces of the tissue maps, which were then fitted on a sigmoid regression curve to calculate the FWHM of the interface (Ahmad *et al* 2015).

Repeatability of tissue property quantification was assessed using same-day test-retest scans. Coefficient of variation (CV), defined as the standard deviation of tissue values divided by the mean, was calculated to analyze variation between independent scans for multiple regions of interest (ROIs) including tumor, liver, muscle, and fat tissue.

Tissue property quantification accuracy was evaluated by mean absolute percentage error (MAPE). This metric was calculated as the pixel-wise difference between the MRF-derived tissue maps and the corresponding ground truth tissue values, averaged across multiple ROIs.

*P* value less than 0.05 was considered statistical significance. Prior studies evaluating the effect of respiratory motion on MRF reported average sample sizes of 9 participants. Given the respiratory motion measurement accuracy of MRF ($0.95 \pm 0.05$) in the pilot study, 22 participants were recruited in the current study to ensure adequate statistical power (Cruz *et al* 2021, Liu *et al* 2023).

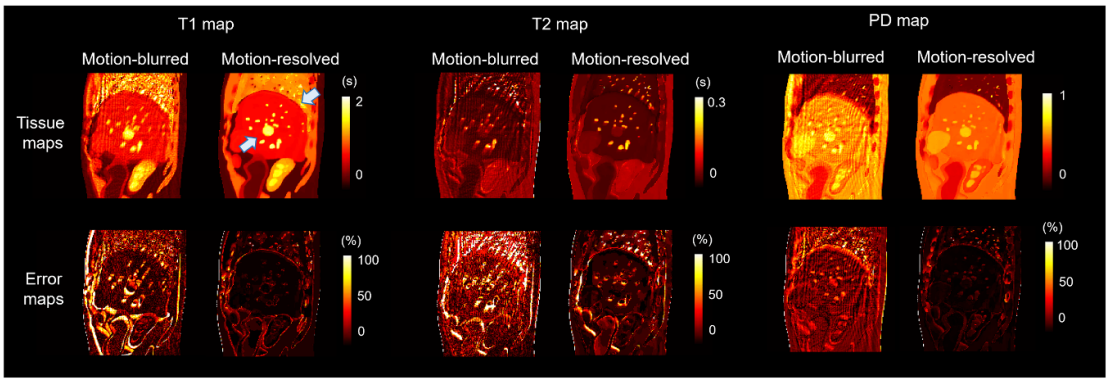


**Figure 2.** MR-MRF results for a representative digital phantom. The top row displays the motion-blurred T1, T2, and proton density (PD) maps (left) alongside the corresponding MR-MRF-derived motion-resolved maps (right). The bottom row shows the error maps for the motion-blurred and motion-resolved parameter estimates.

**Table 3.** The quantitative results of mean absolute percentage error (MAPE) for MR-MRF-derived tissue maps in phantom MRF study.

| | | Mean absolute percentage error (MAPE, %) | | | |
|---|---|---|---|---|---|
| | | Tumor | Liver | Muscle | Fat |
| T1 | Motion-blurred | 18.25 ± 3.12 | 16.01 ± 1.78 | 16.48 ± 3.52 | 36.78 ± 3.52 |
| | Motion-resolved | 9.30 ± 0.92 | 6.31 ± 0.51 | 9.94 ± 0.74 | 13.31 ± 0.74 |
| T2 | Motion-blurred | 29.11 ± 3.78 | 34.61 ± 5.20 | 32.16 ± 2.86 | 28.32 ± 2.86 |
| | Motion-resolved | 8.22 ± 0.79 | 9.12 ± 1.87 | 11.83 ± 1.48 | 11.09 ± 1.48 |
| PD | Motion-blurred | 12.56 ± 1.34 | 13.75 ± 0.58 | 12.83 ± 0.31 | 14.15 ± 0.31 |
| | Motion-resolved | 4.79 ± 1.05 | 4.62 ± 0.67 | 6.49 ± 0.51 | 9.44 ± 0.51 |

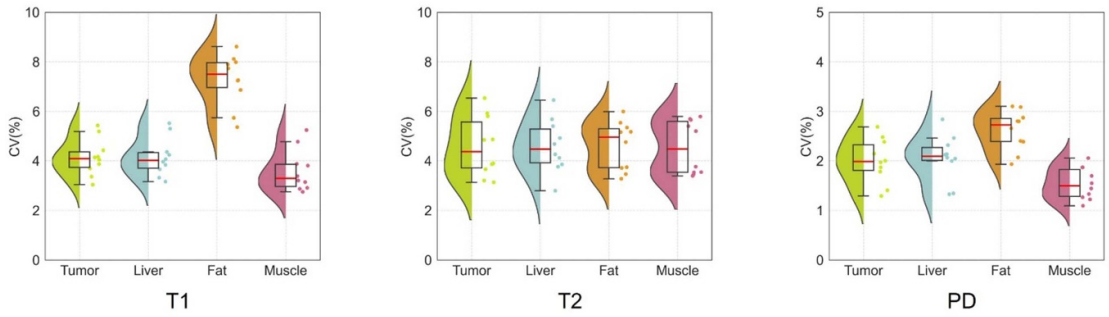


**Figure 3.** The coefficient of variation (CV) for T1, T2, and PD parameters from 10 repeated MR-MRF in the phantom studies.

## 3. Results

### 3.1. Digital phantom MRF study results

Figure 2 shows the T1, T2, and PD maps of a representative phantom. The motion-resolved tissue maps reconstructed using MR-MRF (figure 2, right columns) exhibit well-defined organ boundaries and clear tumor delineation, as indicated by the white arrow. In contrast, the motion-blurred tissue maps (figure 2, left columns) show indistinct organ boundaries and inaccurate tumor appearance due to respiratory motion corruption. The error maps in the second row of figure 2 demonstrate that the MR-MRF method significantly reduces tissue quantification errors compared to the motion-blurred tissue maps. The quantitative results of tissue quantification error are presented in table 3, where MR-MRF exhibits the lowest MAPE error across all organ types. The 10-repetition repeatability results are presented in figure 3. The PD map achieved the lowest CV values, ranging from 1.5% to 4.5% across the different tissue types. The T2 map demonstrated more stable repeatability among all tissue types, with a mean CV of 4.6%. For the T1 map, the tumor, liver, and muscle tissues exhibited relatively similar CV values (3.5%–4.1%), whereas fat presented worse repeatability with a CV of 7.3%.

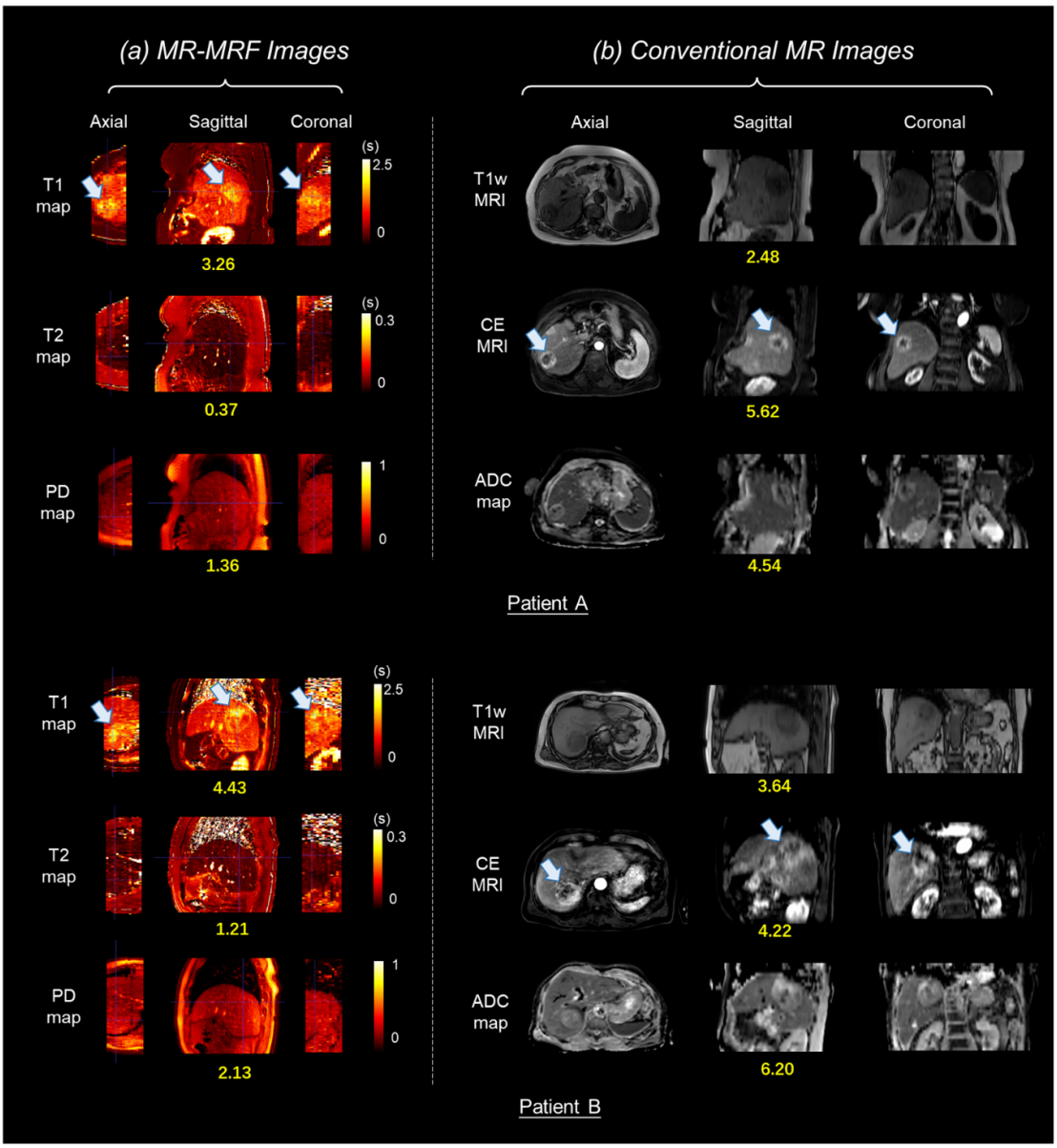


**Figure 4.** Comparison of MR-MRF quantitative tissue mapping with conventional MRI sequences in hepatocellular carcinoma (HCC). Left: MR-MRF-derived parametric maps (T1, T2, and PD) from two representative HCC patients: (A) 75 year-old male and (B) 87 year-old female. Right: corresponding conventional MRI sequences including (i) T1-weighted imaging, (ii) contrast-enhanced MRI (CE-MRI; arterial phase), and (iii) ADC maps. Tumors are indicated by white arrows (T1 maps, CE-MRI), with adjacent yellow text reporting quantitative tumor-to-liver contrast-to-noise ratios (CNR).

### 3.2. *In vivo* MRF study results

Figure 4 demonstrates MR-MRF-derived quantitative maps (T1, T2, and PD) alongside conventional MRI sequences (T1-weighted, CE MRI [CE-MRI], and ADC maps) for two representative patients. Light white arrows mark tumor locations in T1 maps and CE-MRI, with adjacent yellow text denoting tumor-to-liver contrast-to-noise ratios (CNRs). The MR-MRF T1 maps provided clear tumor visualization across all three planes (axial, sagittal, and coronal), while T2 and PD maps showed lower lesion conspicuity. Quantitative analysis revealed the highest CNR in ADC maps ($5.37 \pm 0.83$), followed by CE-MRI ($4.92 \pm 0.70$) and MR-MRF T1 maps ($3.84 \pm 0.59$), all of which outperformed conventional T1-weighted imaging ($3.06 \pm 0.58$).

Figure 5 compares MR-MRF-derived motion-resolved tissue maps with conventional motion-blurred reconstructions. Qualitative analysis (figure 5(a)) reveals substantial motion artifacts along liver-lung boundaries in motion-blurred maps, while MR-MRF processing achieves clear anatomical delineation. Quantitative edge sharpness analysis, performed using three linear profiles at liver-lung interfaces (white dotted lines), demonstrated significantly improved boundary definition in motion-resolved maps (FWHM: $3.1 \pm 1.7$ mm vs $9.9 \pm 3.4$ mm in motion-blurred maps, $p < 0.0001$). Blinded radiologist

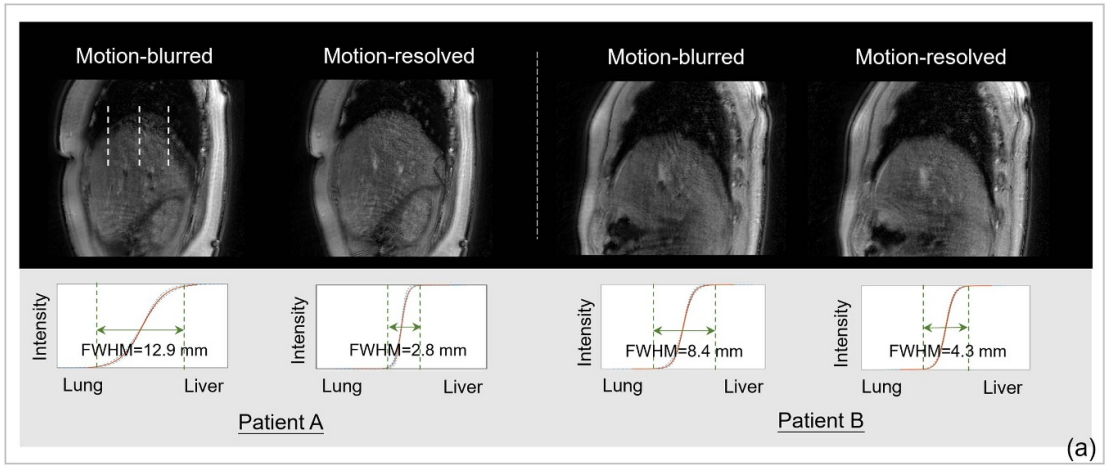


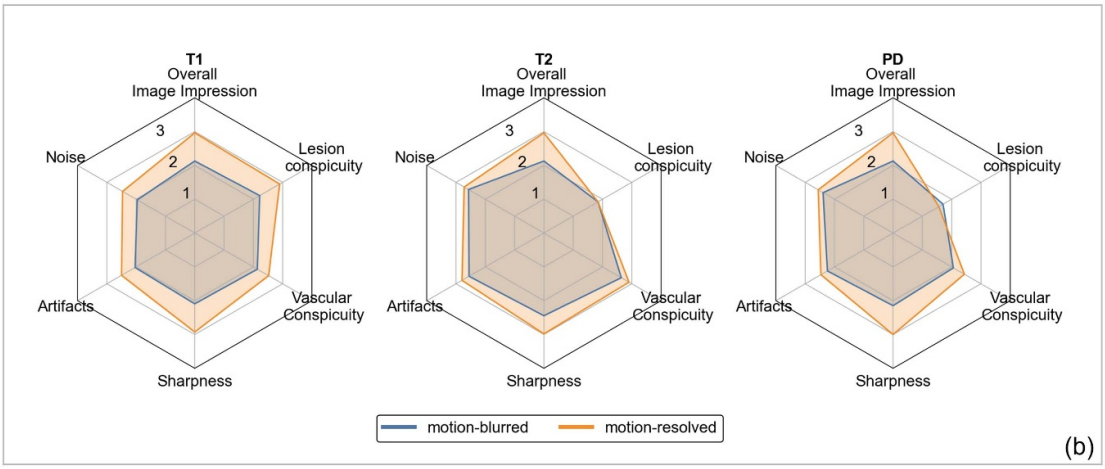


**Figure 5.** Comparison between MR-MRF-derived motion-resolved tissue maps with conventional motion-blurred reconstructions. (a) Representative PD maps from MRF in two hepatocellular carcinoma patients, a 66 year-old male (Patient A) and a 44 year-old male (Patient B). Left columns display motion-blurred PD maps reconstructed from free-breathing acquisitions; right columns show corresponding motion-resolved PD maps processed with MR-MRF. Edge profile analysis (bottom panels) demonstrates improved boundary sharpness in motion-resolved maps, with average liver-lung interface profiles (red curves) and full-width at half-maximum (FWHM) measurements (green double-headed arrows). (b) Blinded radiologist assessment of image quality parameters (overall image impression, noise, artifacts, sharpness, vascular conspicuity, lesion conspicuity) presented as radar plots. Blue-shaded regions represent scores for motion-blurred reconstructions; orange-colored regions indicate superior performance of motion-resolved T1, T2, and PD maps.

assessment showed clinically meaningful improvements: motion-resolved maps received an average score of 3 ('moderate quality, sufficient for diagnosis') versus 2 ('inconclusive, substantially reduced diagnostic confidence') for motion-blurred reconstructions ($p < 0.05$). All quality metrics improved with MR-MRF processing (noise: +20.5%, artifacts: +35.4%, sharpness: +49.3%), with particularly notable gains in T1 map lesion conspicuity (+35.3%). The limited CNR in T2/PD maps precluded significant conspicuity improvements.

Figure 6 presents the test-retest repeatability of the tissue property measurements in the in vivo studies. The correlation plots in figure 6(a) demonstrate a high degree of agreement between the repeated measurements, with coefficients of determination ($R^2$) of 0.964 for T1, 0.800 for T2, and 0.856 for PD. The CV results shown in figure 6(b) provide further insight into repeatability. T1 exhibited the lowest CV values, with mean ± standard deviation of 3.9% ± 3.1% in the tumor, 5.5% ± 7.1% in the liver, 6.1% ± 6.0% in fat, and 3.4% ± 2.4% in muscle. In contrast, the mean CV ranges were higher for T2 (6.9% to 11.8%) and PD (7.1% to 9.8%) across the different tissue regions.

## 4. Discussion

MR-MRF successfully reconstructs motion-resolved tissue property maps at the EOE motion state. Respiratory motion-induced artifacts were eliminated from the free-breathing *k*-space data. The blinded radiologist assessment demonstrated clinically significant improvement in image quality following MR-MRF reconstruction, with mean scores increasing from 2 (indicating 'inconclusive—substantially reduced

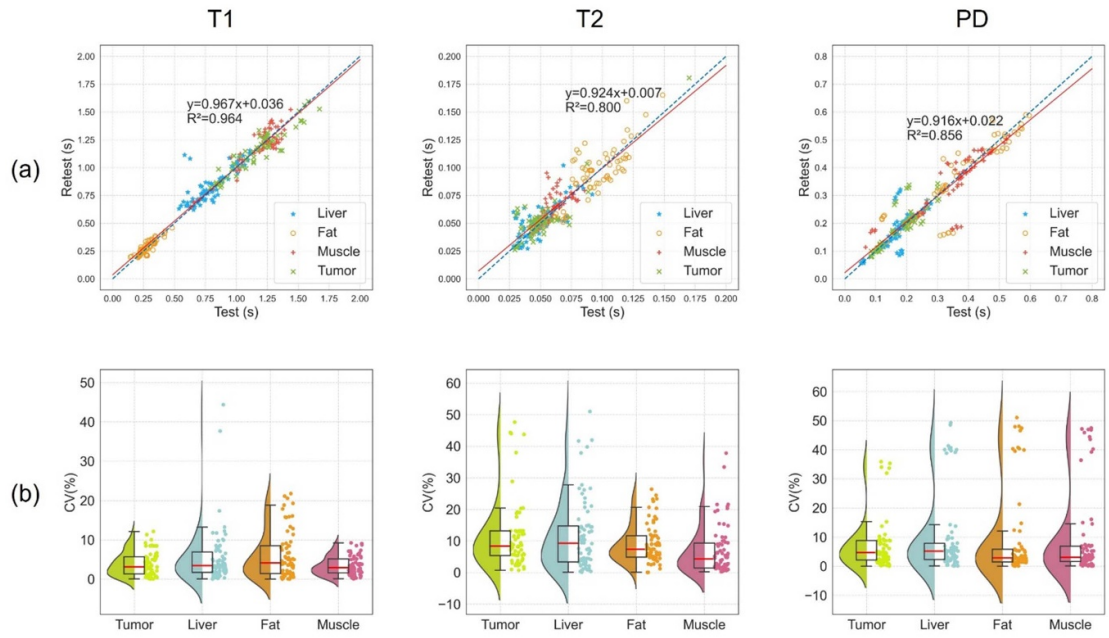


**Figure 6.** Test-retest repeatability results of the in vivo patient studies. (a) The correlation plots of T1, T2, and PD maps obtained from test and retest MRF scans. (b) The CV results of the test-retest repeatability.

diagnostic confidence') to 3 ('moderate quality—sufficient for diagnosis'). Among MR-MRF-derived parametric maps, T1 mapping demonstrated superior tumor-to-liver CNR compared to T2 and PD maps. When evaluated against conventional MRI sequences, T1 maps showed significantly higher CNR than non-contrast T1-weighted imaging and approached the performance of CE-MRI and ADC maps. Notably, this diagnostic-level performance was achieved without contrast agent administration, highlighting MR-MRF's potential as a viable contrast-free alternative for cancer diagnosis. The FWHM of the liver-lung edge in the motion-resolved tissue maps was three times narrower compared to the motion-blurred tissue maps. This suggests the MR-MRF was able to better delineate the organ boundaries despite respiratory motion. However, the FWHM of the MR-MRF-derived PD maps remained slightly larger than the conventional breath-hold images. This discrepancy is likely due to the relatively short acquisition time (3–4 s) of the breath-hold images, which provided high-quality, stable visualization of the anatomy. In contrast, the MR-MRF-derived tissue maps are reconstructed by four-phase (one target and three motion) respiratory sorting scheme. The target phase still encompasses a finite range of respiratory motion. The choice of four phases is a trade-off between respiratory sorting precision and motion modeling accuracy. Increasing the number of discrete motion phases may improve the precision of respiratory sorting. However, this could potentially reduce the quality of anatomical image used for DVF calculation, subsequently degrading the accuracy of the motion modeling itself.

MR-MRF achieved high tissue property quantification repeatability in both phantoms and in vivo studies. To our knowledge, this represents the first investigation of free-breathing MRF repeatability specifically in liver cancer patients. Existing liver MRF studies have been limited to breath-hold protocols and predominantly excluded oncology populations, leaving a critical gap in understanding quantitative MRF's potential for cancer applications (Chen *et al* 2016, Fujita *et al* 2022). The MRF scans were performed on subjects exhibiting varying respiratory motion patterns, with significant differences in respiratory amplitude and frequency across the repeated scans. However, the minimized relative difference of the tissue property values among the repeated scans demonstrates the high robustness of the MR-MRF technique to irregular respiratory motion. Among the different tissue properties quantified, T2 exhibited the lowest repeatability compared to T1 and PD. This is likely due to the inherent lower performance of the MRF sequence in measuring T2, which is known to be more sensitive to B1 field inhomogeneities (Buonincontri and Sawiak 2016). The high repeatability of tissue property quantification demonstrated by the MR-MRF technique may provide important implications for clinical practice. Stable and reliable tissue characterization, particularly of parameters like T1 and PD that exhibited the most consistent repeatability, can provide valuable quantitative biomarkers for longitudinal assessment of treatment response. The ability to directly compare quantitative tissue properties across serial examinations would offer valuable insights into disease biology and treatment mechanisms, ultimately enhancing the

clinical utility of quantitative MRI. Furthermore, the robust spatial registration of MR-MRF-derived tissue maps could facilitate precise tumor localization to guide targeted interventions. It should be noted that the generalizability of MR-MRF is limited by the study's focus on a HCC patient cohort. Future studies should therefore validate and extend the MR-MRF technique to other prevalent liver pathologies, such as fibrosis and steatosis, to assess its broader diagnostic utility.

While the current study establishes the technical feasibility of MR-MRF, its clinical translation requires addressing key limitations inherent in the present implementation. A primary constraint is the use of a multi-slice 2D MRF sequence, which restricts through-plane resolution and prolongs the total acquisition time. Therefore, a natural extension of this work is to develop an accelerated 3D MRF sequence, which would provide isotropic resolution and whole-liver coverage within a clinically acceptable scan time. In addition, while GPU acceleration has been implemented in MR-MRF, the time of current workflow (approximately 15 min for acquisition and 30 min for reconstruction) remains prohibitive long for routine diagnostic and treatment decision-making. Deep learning has demonstrated remarkable efficiency in accelerating the MRF acquisition and reconstruction. First, deep learning model has the ability to generate high-quality brain tissue maps using only 1/10 of the conventional MRF dynamics, which directly corresponds to a tenfold reduction in acquisition time (Chen *et al* 2020). Second, deep learning models achieve second level tissue map reconstruction, which is critical for enabling real-time clinical assessment (Fang *et al* 2019, Li and Hu 2023, 2024). While these approaches have not yet been validated for abdominal/liver MRF—where motion and complex tissue composition add further complexity—it represents a crucial future direction. Finally, to fully establish the clinical diagnostic value, necessary progression of this work is to conduct LI-RADS-based diagnostic reader studies with radiologists, calculate lesion-level diagnostic accuracy metrics (AUC, sensitivity, specificity), and pursue histopathologic correlation in large-scale patient cohorts.

## 5. Conclusion

This study establishes the technical foundation of MR-MRF to achieve repeatable and quantitative liver T1/T2/PD mapping under free-breathing conditions at 3 T. The results validate the feasibility of addressing respiratory motion in abdominal multi-parametric quantitative MRI. To translate this prototype into a potential clinical tool, future work should focus on three critical developments, including accelerated 3D acquisitions to enable volumetric assessment, optimized reconstruction for practical imaging times, and rigorous diagnostic studies to evaluate its added clinical value.

## Data availability statement

The data cannot be made publicly available upon publication because no suitable repository exists for hosting data in this field of study. The data that support the findings of this study are available upon reasonable request from the authors.

## Funding statement

This research was partly supported by National Natural Science Foundation of China (NSFC) Young Scientist Fund (82202941), General Research Funds of University Grants Committee in Hong Kong SAR (GRF 15104323, GRF 15102219, GRF 15104822), Health and Medical Research Fund in Hong Kong (HMRF 10211606, HMRF 12231546), Early Career Scheme of University Grants Committee in Hong Kong SAR (ECS 25100525) and the Innovation and Technology Support Programme of Innovation and Technology Commission in Hong Kong SAR (ITS/049/22FP).

## Ethical statements

This study was performed in line with the principles of the Declaration of Helsinki. The institutional review board (IRB) of the University of Hong Kong and Hospital Authority Hong Kong West Cluster (IRB Number: UW 22-780). Written informed consents were obtained from all individual participants.

## Author contributions

Chenyang Liu 0000-0002-3362-7534
Conceptualization (equal), Data curation (equal), Methodology (lead), Project administration (lead), Writing – original draft (lead), Writing – review & editing (lead)

Tian Li 0000-0003-2344-4336
Project administration (equal), Supervision (supporting)

Lu Wang 0000-0003-4698-1580
Investigation (equal), Resources (equal)

Yat-Lam Wong
Data curation (equal), Investigation (equal)

Mandi Wang
Validation (equal), Visualization (equal)

Huiqin Zhang
Investigation (equal), Validation (equal), Visualization (equal)

Zuojun Wang
Investigation (equal), Visualization (equal)

Haonan Xiao
Visualization (equal), Writing – original draft (equal)

Shaohua Zhi
Investigation (equal), Visualization (equal)

Wen Li
Visualization (equal), Writing – original draft (equal)

Jiang Zhang 0000-0001-5807-1686
Formal analysis (equal)

Xinzhi Teng
Methodology (equal)

Victor Ho-fun Lee
Methodology (equal)

## References

Ahmad R, Ding Y and Simonetti O P 2015 Edge sharpness assessment by parametric modeling: application to magnetic resonance imaging *Concepts Magn. Reson. A* **44** 138–49

Assländer J, Cloos M A, Knoll F, Sodickson D K, Hennig J and Lattanzi R 2018 Low rank alternating direction method of multipliers reconstruction for MR fingerprinting *Magn. Reson. Med.* **79** 83–96

Buonincontri G and Sawiak S J 2016 MR fingerprinting with simultaneous B1 estimation *Magn. Reson. Med.* **76** 1127–35

Cao P, Wang Z, Liu C, Li T, Hui E S and Cai J 2022 Motion-resolved and free-breathing liver MRF *Magn. Reson. Imaging* **91** 69–80

Chen D, Davies M E and Golbabaee M 2020 Compressive MR fingerprinting reconstruction with neural proximal gradient iterations *Int. Conf. on Medical Image Computing and Computer-Assisted Intervention* (Springer)

Chen Y, Jiang Y, Pahwa S, Ma D, Lu L, Twieg M D, Wright K L, Seiberlich N, Griswold M A and Gulani V 2016 MR fingerprinting for rapid quantitative abdominal imaging *Radiology* **279** 278–86

Cruz G, Qi H, Jaubert O, Kuestner T, Schneider T, Botnar R M and Prieto C 2021 Generalized low-rank nonrigid motion-corrected reconstruction for MR fingerprinting *Magn. Reson. Med.* **87** 746–63

Fang Z, Chen Y, Liu M, Xiang L, Zhang Q, Wang Q, Lin W and Shen D 2019 Deep learning for fast and spatially constrained tissue quantification from highly accelerated data in magnetic resonance fingerprinting *IEEE Trans. Med. Imaging* **38** 2364–74

Fujita S *et al* 2022 MR fingerprinting for liver tissue characterization: a histopathologic correlation study *Radiology* **306** 220736

Golbabaee M, Buonincontri G, Pirkl C M, Menzel M I, Menze B H, Davies M and Gómez P A 2021 Compressive MRI quantification using convex spatiotemporal priors and deep encoder-decoder networks *Med. Image Anal.* **69** 101945

Huang S S, Boyacioglu R, Bolding R, MacAskill C, Chen Y and Griswold M A 2021 Free-breathing abdominal magnetic resonance fingerprinting using a pilot tone navigator *J. Magn. Reson. Imaging* **54** 1138–51

Jaubert O, Arrieta C, Cruz G, Bustin A, Schneider T, Georgiopoulos G, Masci P-G, Sing-Long C, Botnar R M and Prieto C 2020 Multi-parametric liver tissue characterization using MR fingerprinting: simultaneous $T_1$, $T_2$, $T_2^*$, and fat fraction mapping *Magn. Reson. Med.* **84** 2625–35

Jiang Y, Ma D, Seiberlich N, Gulani V and Griswold M A 2015 MR fingerprinting using fast imaging with steady state precession (FISP) with spiral readout *Magn. Reson. Med.* **74** 1621–31

Li P and Hu Y 2023 Learned tensor low-CP-rank and Bloch response manifold priors for non-Cartesian MRF reconstruction *IEEE Trans. Med. Imaging* **42** 3702–14

Li P and Hu Y 2024 Deep magnetic resonance fingerprinting based on local and global vision transformer *Med. Image Anal.* **95** 103198

Li T, Cui D, Hui E S and Cai J 2020 Time-resolved magnetic resonance fingerprinting for radiotherapy motion management *Med. Phys.* **47** 6286–93

Liu C *et al* 2023 Respiratory-correlated four-dimensional magnetic resonance fingerprinting (RC-4DMRF) for liver cancer radiotherapy motion management *Int. J. Radiat. Oncol. Biol. Phys.* **117** 493–504

Ma D, Gulani V, Seiberlich N, Liu K, Sunshine J L, Duerk J L and Griswold M A 2013 Magnetic resonance fingerprinting *Nature* **495** 187–92

MacAskill C J et al 2021 Rapid B1-insensitive MR fingerprinting for quantitative kidney imaging *Radiology* **300** 380–7
McGivney D F, Pierre E, Ma D, Jiang Y, Saybasili H, Gulani V and Griswold M A 2014 SVD compression for magnetic resonance fingerprinting in the time domain *IEEE Trans. Med. Imaging* **33** 2311–22
Panta R K, Segars P, Yin F-F and Cai J 2012 Establishing a framework to implement 4D XCAT phantom for 4D radiotherapy research *J. Cancer Res. Ther.* **8** 565–70
Poorman M E, Martin M N, Ma D, McGivney D F, Gulani V, Griswold M A and Keenan K E 2020 Magnetic resonance fingerprinting part 1: potential uses, current challenges, and recommendations *J. Magn. Reson. Imaging* **51** 675–92
Segars W P, Sturgeon G, Mendonca S, Grimes J and Tsui B M 2010 4D XCAT phantom for multimodality imaging research *Med. Phys.* **37** 4902–15
Segars W P, Tsui B M W, Cai J, Yin F-F, Fung G S K and Samei E 2018 Application of the 4-D XCAT phantoms in biomedical imaging and beyond *IEEE Trans. Med. Imaging* **37** 680–92
Vishnevskiy V, Gass T, Szekely G, Tanner C and Goksel O 2017 Isotropic total variation regularization of displacements in parametric image registration *IEEE Trans. Med. Imaging* **36** 385–95
Wang Z, Li H, Zhang Q, Yuan J and Wang X 2016 Magnetic resonance fingerprinting with compressed sensing and distance metric learning *Neurocomputing* **174** 560–70
Weigel M 2015 Extended phase graphs: dephasing, RF pulses, and echoes—pure and simple *J. Magn. Reson. Imaging* **41** 266–95
Xiao H *et al* 2022 A dual-supervised deformation estimation model (DDEM) for constructing ultra-quality 4D-MRI based on a commercial low-quality 4D-MRI for liver cancer radiation therapy *Med. Phys.* **49** 3159–70